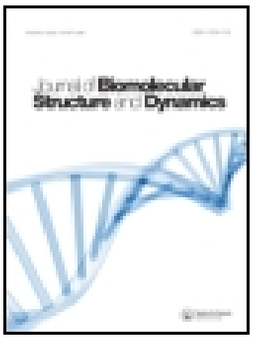

Journal of Biomolecular Structure and Dynamics

ISSN: (Print) (Online) Journal homepage: https://www.tandfonline.com/loi/tbsd20

Synthesis, molecular docking and dynamics studies of pyridazino[4,5-*b*]quinoxalin-1(2*H*)-ones as targeting main protease of COVID-19

Parvin Moghimi, Hossein Sabet-Sarvestani & Ali Shiri

To cite this article: Parvin Moghimi, Hossein Sabet-Sarvestani & Ali Shiri (2023): Synthesis, molecular docking and dynamics studies of pyridazino[4,5-*b*]quinoxalin-1(2*H*)-ones as targeting main protease of COVID-19, Journal of Biomolecular Structure and Dynamics, DOI: 10.1080/07391102.2023.2191127

To link to this article: https://doi.org/10.1080/07391102.2023.2191127

JOURNAL OF BIOMOLECULAR STRUCTURE AND DYNAMICS
https://doi.org/10.1080/07391102.2023.2191127

Synthesis, molecular docking and dynamics studies of pyridazino[4,5-*b*]quinoxalin-1(2*H*)-ones as targeting main protease of COVID-19

Parvin Moghimi, Hossein Sabet-Sarvestani and Ali Shiri

Department of Chemistry, Faculty of Science, Ferdowsi University of Mashhad, Mashhad, Iran

Communicated by Ramaswamy H. Sarma

ABSTRACT

The COVID-19 pandemic caused by severe acute respiratory syndrome coronavirus 2 (SARS-CoV-2) has created a crisis in public health. Because, the $3CL^{pro}$, the main protease of SARS-CoV-2, possesses a critical role in coronavirus replication, many efforts have been devoted to developing various inhibitors to prevent the fast spread of COVID-19. In the current work, a number of various pyridazino[4,5-*b*]quinoxalin-1(2*H*)-one derivatives bearing thiadiazine and thiadiazole fragments has been prepared via a straightforward and practical strategy involving the reaction of 2-(ethoxycarbonyl)-3-formylquinoxaline 1,4-dioxide with thiocarbohydrazide under reflux conditions. To determine the bioavailability of pyridazino[4,5-*b*]quinoxalin-1(2*H*)-one derivatives, Lipinski's rule of five has been carried out. Regarding this rule, none of the synthesized compounds exhibit any deviation from Lipinski's rule of five. Furthermore, molecular docking and molecular dynamics approaches have been implemented to figure out the potential interactions of products with SARS-CoV-2 main protease. The outcomes of molecular docking studies demonstrate that the phenyl and nitrophenyl substituted pyridazino[4,5-*b*]quinoxalin-1(2*H*)-one show the lowest binding affinity among the other compounds, indicating a favorable orientation in the active site of the chymotrypsin-like cysteine protease. In addition, the MD simulation performed to evaluate the stability of the protein–ligand complex represents that the average binding energy of the nitrophenyl complex is less than that of the phenyl complex. Therefore, according to the *in silico* results, the inhibitory effect of the nitrophenyl complex is more significant than the phenyl complex.

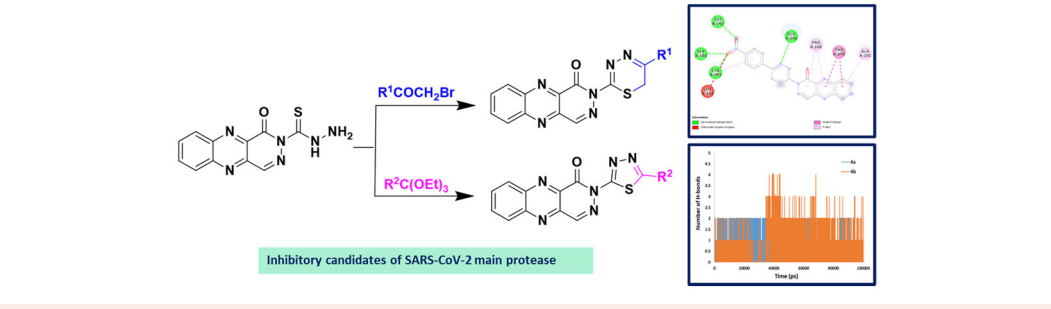

ARTICLE HISTORY
Received 21 June 2022
Accepted 15 January 2023

KEYWORDS
Pyridazinoquinoxaline; COVID-19; inhibitors of SARS-CoV-2; molecular docking; molecular dynamics

1. Introduction

One of the most controversial problems around the world is the COVID-19 pandemic. This severe acute respiratory syndrome coronavirus 2 (SARS-CoV-2) has attracted significant research towards the development of vaccines and antiviral therapeutics (Wu et al., 2020). The main protease of SARS-CoV-2 is named 3-chymotrypsin-like cysteine protease ($3CL^{pro}$), has three domains: domain I (1–101) and domain II (102–184) consisting of a β-barrel, while domain III (201–303) possesses α-helices. The $3CL^{pro}$ active site, which contains Cys 145 and His 41 amino acids residues, is situated between domains I and II. This protease is an attractive drug targeting because of its essential role in cleaving polyproteins and releasing the vital proteins for viral replication (Wang et al., 2016; Zhang et al., 2020). Therefore, a vast number of medical research has been directed to develop potential inhibitors against the coronavirus $3CL^{pro}$. According to pharmacophore studies, several of the SARS-CoV-2 main protease inhibitors such as α-ketoamide, aldehyde compounds, octahydroisochromene and natural flavonoid interact with the catalytic dyad residues His41 and Cys145 of $3CL^{pro}$ through hydrogen bonds and hydrophobic interactions (Dai

CONTACT Ali Shiri alishiri@um.ac.ir Department of Chemistry, Faculty of Science, Ferdowsi University of Mashhad, Mashhad, Iran.
Supplemental data for this article can be accessed online at http://dx.doi.org/10.1080/07391102.2023.2191127.

et al., 2020; Gentile et al., 2020; Silva Arouche et al., 2020; Yoshizawa et al., 2020; Zhang et al., 2020).

Over the past two decades, many studies reported that nitrogen-containing heterocyclic molecules exhibited many biological and pharmaceutical properties, such as high inhibitory and antiviral activity (Sun et al., 2020; Vitaku et al., 2014). Since the emergence of COVID-19 crises, the structural features of N-heterocyclic compounds have gained prominence in discovering potent non-covalent inhibitors against the SARS-CoV-2 main protease (Assis et al., 2021; Liu et al., 2020; Llanes et al., 2020; Ton et al., 2020).

Quinoxaline consists of a pyrazine ring in conjunction with a benzene ring, known as an essential class of heterocyclic system (Montana et al., 2019). Compounds that possess quinoxaline core exhibit a broad range of biological activities in medicinal chemistry, therapeutics and pharmacology, including antiviral (El-Tombary & El-Hawash, 2014), anticancer (Tseng et al., 2016), antibacterial (Keivanloo et al., 2020), antimalarial (Guillon et al., 2017), anti-HIV (Fabian et al., 2020) and inhibitory activity toward hepatitis C virus (HCV) protease (Nageswara Rao et al., 2021). In addition, a number of quinoxaline derivatives have been identified as potent inhibitors of the SARS-CoV-2 main protease (Chemboli et al., 2021; Divya et al., 2022; El Bakri et al., 2021). Consequently, the synthesis of quinoxaline derivatives and assessment of their cytotoxic and antiviral activities against a variety of RNA and DNA viruses is one of the hottest areas of study. During the last decade, the synthesis of substituted pyridazinones has gained a great deal of attention due to their powerful anti-inflammatory (Asif, 2015), vasodilatory activity (Bansal et al., 2009), platelet aggregation inhibitors (Thota & Bansal, 2010), anti-cancer (Malinka et al., 2004), antithrombotic (Avcı et al., 2015) and antiviral properties (Li et al., 2015). The pyridazinoquinoxaline derivatives, an important heterocyclic compound bearing quinoxaline and pyridazine moiety, exhibit several significant pharmaceutical and biological properties, such as antibacterial and anti-inflammatory activities (Abouzid et al., 2010; de Lucio et al., 2022). Few strategies have been reported to prepare pyridazinoquinoxaline scaffolds, which involve the reaction of 3-aroylmethyl-2-(trifluoromethyl)quinoxalines with excess amounts of hydrazine hydrate and the reaction of 2-(1-methylhydrazino)quinoxaline *N*-oxide with β-diketones (Kurasawa et al., 2005; 2007; Kurasawa & Kim, 2002; Sosnovskikh et al., 2016). According to our knowledge, neither the use of thiocarbohydrazide in the preparation of pyridazinoquinoxaline, nor the investigation of this structure as an inhibitor of the SARS-CoV-2 main protease have been reported. As a continuation of our previous studies (Bigonah-Rasti et al., 2020; Kohandel et al., 2021; Moghimi et al., 2022; Sheikhi-Mohammareh et al., 2020; Sheikhi-Mohammareh & Shiri, 2018), and in an attempt to develop new inhibitors targeting COVID-19 main protease, we report a one-pot strategy that includes cyclization and reduction to construct pyridazino[4,5-*b*]quinoxalin-1(2*H*)-one scaffold in good yield. Furthermore, thiadiazine, and thiadiazole fragments, which exhibit anti-coronavirus activity (Jilloju et al., 2022; Petrou et al., 2022), were also employed to provide more favorable inhibitory activity against the main protease of COVID-19. Thus, a series of pyridazino[4,5-*b*]quinoxalin-1(2*H*)-ones have been prepared in good yields and their inhibitory activity against the 3-chymotrypsin-like cysteine protease of SARS-CoV-2 evaluated by a combination of molecular docking and molecular dynamics simulations. According to the findings of molecular docking, compounds **4a** and **4b** had the lowest binding affinities, indicating a favorable orientation in the active site of the chymotrypsin-like cysteine protease. To gain insight into ligand–protein interactions, the molecular docking results were utilized as inputs for molecular dynamics simulations. The MD simulation showed that compound **4b** has more inhibitory effects than compound **4a** because its averaged binding energy value is lower.

2. Result and discussion

In a continuing effort to synthesize new inhibitors of SARS-CoV-2 main protease, 2-(ethoxycarbonyl)-3-formylquinoxaline 1,4-dioxide **1** was first synthesized according to the published procedures (Barriga-González et al., 2020; Jaso et al., 2005; Monge et al., 1995). Also, regarding the reported literature thiocarbohydrazide **2** was produced (Sherif & Ahmed, 2010). Initially, the reaction between compound **1** and thiocarbohydrazide **2** was conducted in the presence of ethanol under reflux conditions to produce 1-oxopyridazino[4,5-*b*]quinoxaline-2(1*H*)-carbothiohydrazide **3**. Since, amine groups like hydrazine hydrate and phenylhydrazine can reduce 3-phenylquinoxaline-2-carboxylate 1,4-di-*N*-oxide systems into the corresponding quinoxaline (Lima et al., 2008; Vega et al., 1984). The thiocarbohydrazide **2** can also act both as a nucleophile and reducing agent to afford the desired quinoxaline derivative **3** (Scheme 1).

Based on the reaction conditions and substitution pattern, the cyclo-condensation of compound (**3**) with various phenacyl bromides in ethanol under reflux conditions gave the corresponding 2-(5-phenyl-6*H*-1,3,4-thiadiazin-2-yl)pyridazino[4,5-*b*]quinoxalin-1(2*H*)-one derivatives (**4a–e**) in good yields (Table 1).

Furthermore, the treatment of compound **3** with various triethylorthoesters in boiling acetic acid led to the formation of desired (**5a–c**) products bearing thiadiazol rings (Table 2). The structural assignment of compounds (**4a–e**) and (**5a–c**) characterized by spectroscopic and microanalytical data were in agreement. Moreover, computational investigations such as ADME studies, molecular docking and molecular dynamics have been conducted to evaluate synthesized molecules as potential SARS-CoV-2 main protease inhibitors.

3. Computational analyses

3.1. ADME studies

Drug development is a complex, ambiguous and time-consuming procedure that can be divided into various steps. Evaluating ligand–receptor interaction is a key step in all drug design and discovery approaches. The limitation of animal models in the investigation of synthesized compounds as safe drug candidates causes an increase in the popularity

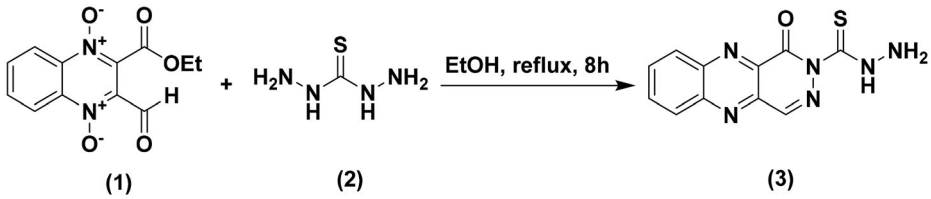

Scheme 1. Construction of 1-oxopyridazino[4,5-b]quinoxaline-2(1H)-carbothiohydrazide.

Table 1. Synthetic route for the construction of 2-(5-phenyl-6*H*-1,3,4-thiadiazin-2-yl)pyridazino[4,5-*b*]quinoxalin-1(2*H*)-ones.

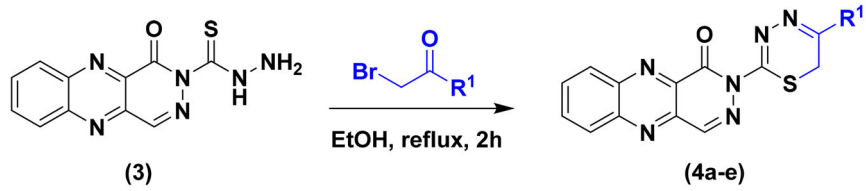

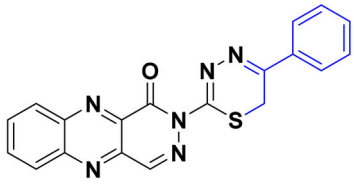

4a 67%

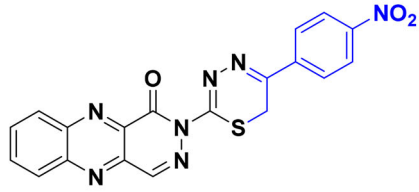

4b 71%

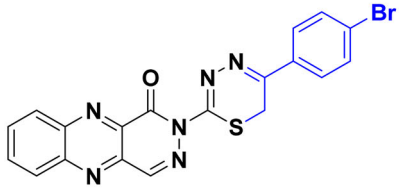

4c 64%

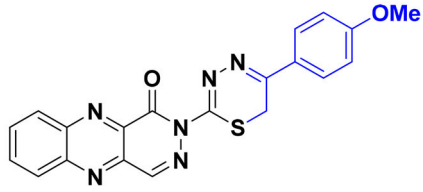

4d 73%

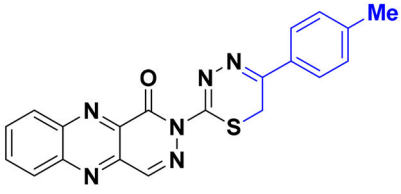

4e 65%

of computational tools (Brogi et al., 2020). Thus, computational approaches, based on *in silico* methodologies, have been considered a primary requirement in pharmaceutical sciences. Discovering new biological targets, proper for treating new diseases, should be accomplished by introducing novel organic molecules or reusing old drugs against new pathogens. Also, pharmacokinetic issues have a linear relationship with the used costs and time. To overcome these problems, *in silico* physicochemical and pharmacokinetic investigations are essential. Thus, unfavorable efficacy and safety, caused mainly by absorption, distribution, metabolism and excretion (ADME) characters, lead to the elimination of many candidate drugs in the final step.

Table 3 illustrates the results of ADME analyses by the SwissADME server (Daina et al., 2017), including the number of the hydrogen-bond donor, the number of the hydrogen-bond acceptor, molecular weight, molar refractivity, logarithms of octanol/water partition coefficient (log*P*) and topological polar surface area (TPSA). Moreover, the results of PAINS (Pan-Assay Interference Compounds) analysis, were applied to specify the possibility of a molecule being toxic. Zero values of PAINS structural alerts reveal a non-toxic character for a corresponding compound (Isa et al., 2020). The analyses are carried out regarding the applied bioavailability during the procedure of drug discovery. Various rules have been used to figure out the bioavailability of a molecule. Lipinski's rule of five is one of the best viewpoints to characterize appropriate membrane permeability and oral bioavailability. Also, the rule is used to determine efficient gastrointestinal absorption in the human abdomen. In

Table 2. Synthetic route for the construction of 2-(5-alkyl-1,3,4-thiadiazol-2-yl)pyridazino[4,5-*b*]quinoxalin-1(2*H*)-ones.

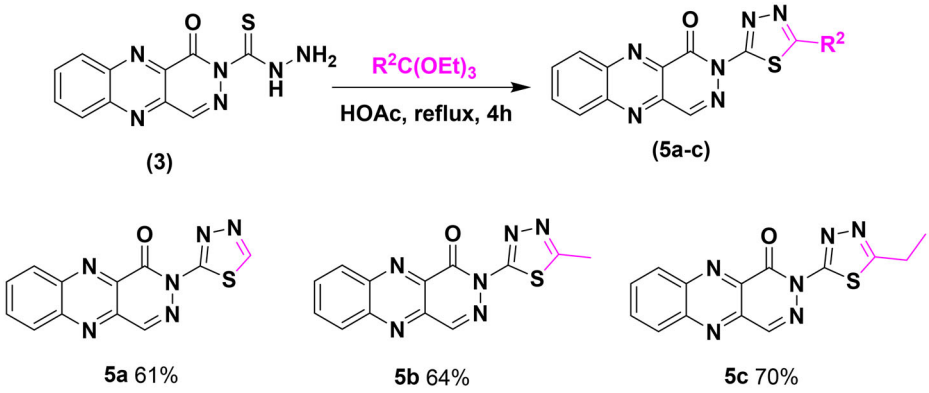

respect of the Lipinski rule, good bioavailability for a typical compound is provided with the molecular weight (MW) $\leq$ 500, the value of log*P* $\leq$ 4.15, number of hydrogen bond donors $\leq$ 5, number of hydrogen-bond acceptor $\leq$ 10 (Padilla-Salinas et al., 2020). Ghose rule suggests 160 $\leq$ MW $\leq$ 480, $-0.4 \leq$ log*P* $\leq$ 5.6, the value of molar refractivity (MR) 40 $\leq$ MR $\leq$ 130, and the number of atoms 20 $\leq n \leq$ 70 for a compound having good bioavailability. As shown in Table 3, the synthesized compounds do not show any violation of the Lipinski Rule of Five, which reveals their drug-like potentiality.

3.2. Methodology

3.2.1. Molecular docking

Molecular docking is a unique tool to investigate how the ligands and receptors fit together and how the enzymes interact with the ligands (Dolatkhah et al., 2017). In drug discovery investigation, molecular docking is carried out to establish a structure–activity relationship and to study the interaction of the synthesized compound and enzyme active site. In our investigation, a deposited complex form of the 3D crystal structure of the main protease of SARS-CoV-2 bearing an inhibitor called **N3** on the RCSB protein data bank (PDB ID: 6LU7) was applied, which was reported by Yang and coworkers (Jin et al., 2020). After removing the inhibitor and water molecules, missing atoms were corrected by Chimera and Notepad++ (Pettersen et al., 2004), and the clean enzyme was used for molecular docking investigation and molecular simulations. The amino acids in the binding site of the enzyme were determined by the BIOVIA Discovery Studio Visualizer (discovery-studio-visualizer-download). Docking calculations were performed by AutoDock-Vina software (Trott & Olson, 2010). Before running the molecular docking process, polar hydrogen atoms and charges were added to the cleaned enzyme then the AutoDock Tools was applied to convert the PDB format to the Partial Charge and Atom Type (PDBQT) format. Also, all the synthesized molecules were optimized using Gaussian 09 (Frisch et al., 2009) software by B3LYP/6-31G(d,p) level of theory. Similarly, PDBQT formats of the optimized ligands were produced after considering polar hydrogen atoms and Gasteiger charges by AutoDock Tools. The applied grid box size for all the docking investigations is 60 Å $\times$ 60 Å $\times$ 60 Å centralized on the respective geometric center. The Cartesian coordinates of the grid box were centered on the $x = -14.212$; $y = 19.133$; $z = 64.83$ coordinates of the enzyme. The energy values of confirmation were determined for 20 geometry conformers by a genetic algorithm called Lamarckian algorithm (Bofill, 1995). In this method, a population of the conformations is produced and was ranked according to the binding energy values in kcal.mol^{-1}.

3.2.2. Molecular dynamics simulation

The best conformers of the docking analyses for compounds **4a** and **4b** were extracted to molecular dynamic simulation via the AMBER99SB-ILDN force field in Gromacs2020 (Abraham et al., 2015). A cubic box with simple point charge (SPC) (Berendsen et al., 1981) water was used to solve the docked complex, and Na^+ or Cl^- counter ions were added to the system for the overall electrostatic neutrality. The effect of long-range electrostatic interactions was evaluated by Particle Mesh Ewald (PME) method with a direct space cut-off of 1.2 nm and Fourier grid spacing of 0.16 nm (Yuan et al., 2013). The cutoff distance was considered 1.2 Å for the long-range van der Waals (VDW) energy. The temperature and pressure during the time of simulation were readjusted by a V-rescale thermostat (Bussi et al., 2007) and Parrinello-Rahman barostat (Parrinello & Rahman, 1981), respectively, in which pressure coupling at 1 atm and temperature coupling at 298.15 K with 2-ps time step were used.

Firstly, energy minimization of the whole system was carried out without any restraint for 50,000 iteration steps by the steepest descent algorithm (Petrova & Solov'ev, 1997). Then, the systems reached an equilibrium state through two distinct simulation steps. In the first stage, the systems were equilibrated by a constant number of particles, volume and temperature, NVT ensemble approach (Zhang et al., 2013), during 200 ps simulation at 310 K, whereat the Verlet scheme was assigned to control the temperature. In the same simulation time, the second stage of equilibration was performed through a constant number of particles, pressure and temperature, NPT ensemble protocol (Zhang et al., 2013), at 300 K, in which Berendsen barostat and Verlet scheme (Elmore & Dougherty, 2001) were applied to control pressure

Table 3. Calculated physiochemical properties, lipophilicity, water-solubility, pharmacokinetics, drug-likeness and bioactivity score of the synthesized compounds by SwissADME.

Compound	Log *S* Log (mol/l)	Heavy atoms	MW (g/mol)	Rotatable bonds	H-bond acceptors	H-bond donors	Log $P_{o/w}$ (iLOGP)	Molar refractivity	TPSA Å^2	Bioavailability score	PAINS	Lipinski violation
3	−2.48	19	272.29	2	5	2	1.56	73.66	130.81	0.55	0	0
4a	−4.57	27	372.40	2	6	0	2.21	113.96	110.69	0.55	0	0
4b	−4.63	30	417.40	3	8	0	1.97	122.78	156.51	0.55	0	0
4c	−5.48	20	451.30	2	6	0	2.72	121.66	110.69	0.55	0	0
4d	−4.64	29	402.43	3	7	0	2.60	120.45	119.92	0.55	0	0
4e	−4.87	28	386.43	2	6	0	2.55	118.93	110.69	0.55	0	0
5a	−2.97	20	282.28	1	6	0	1.55	73.90	114.69	0.55	0	0
5b	−3.28	21	296.31	1	6	0	1.86	78.87	114.69	0.55	0	0
5c	−3.54	22	310.33	2	6	0	2.12	83.68	114.69	0.55	0	0

(constant to 1 Bar) and to control temperature, respectively. LINCS algorithm was used to evaluate covalent bond restrictions in the equilibration steps (Yuan et al., 2012). After that, the ultimate production step was accomplished for 100 ns of MD simulation under a constant temperature of 300 K, in which the simulation trajectories were saved for every 1 fs. The MD simulation was replicated three times for each complex and the mean values of the obtained parameters were applied to structural analysis.

The results illustrated that the synthesized structures had a different interaction with the corresponding amino acids in the active site of the enzyme; the interacting amino acids and corresponding binding energies of all structures are shown in Table 4, in which compounds **4a** and **4b** have the lowest binding energy (−7.6 kcal/mol). Also, the calculated binding energy of the embedded **N3** molecule, as a reference (**Ref**) inhibitor, is larger (−6.4 kcal/mol) than all the synthesized structures. Thus, docking investigations reveal that the synthesized compounds are more powerful inhibitors than the **N3** molecule. Figure 1 shows the binding modes of **4a** and **4b** compounds and the interacting residues with these compounds.

3.3. Molecular simulation results

The root mean square deviation (RMSD), as a structural stability criterion of the complexes during the simulation, was performed to evaluate the average change in displacement that occurred in protein and ligand (Figure 2). RMSD value for frame X can be represented by Eq. (1) (Bharadwaj et al., 2021).

$$\mathrm{RMSD_X} = \sqrt{\frac{1}{N}\sum_{i=1}^{N}\left(r_i'(t_x) - r_i(t_{\mathrm{ref}})\right)^2} \ldots \quad (1)$$

In which, N represents the number of atoms, t_{ref} is defined as the reference time at 0 interval, and r′ is marked as the position of the atoms in frame X after superimposition on the reference frame at interval t_x. RMSD plots depict the stability and conformation changes of the main protease and its complex forms with **4a** and **4b** during the simulation. Mean RMSD values between 0.1 and 0.3 nm can be considered good and acceptable values (Diallo et al., 2021). Nevertheless, higher values of more than 0.3 nm are rejected.

As shown in the RMSD plot in Figure 2, almost all three replications of MD simulation, called MD(1), MD(2) and MD(3), respectively, for the **4a** complex get an equilibrium state after 30,000 ps of the simulation and is stable up to 100,000 ps. The average RMSD values of MDs 1–3, for this complex are 0.33, 0.26 and 0.34 (nm), respectively. The average value of these numbers is 0.31 nm. RMSD plot of **4b** complex for the first and second replications shows an equilibrium state after 10,000 ps which is stable up to 100,000 ps. However, in the case of the third replication, RMSD values increase between 33,000 and 78,000 ps, after this period, the growth is ceased and the complex gets an equilibrium until 100000 ps. The results of averaged RMSD values for MDs 1–3 are 0.22, 0.25 and 0.35 nm, respectively, which mean value of them is 0.27 nm. Thus, it can be concluded that the acquired equilibrium for the complexion of the ligand **4b** with the main-protease is more lasting than **4a** one.

Moreover, RMSF calculation is helpful in the specification of local fluctuations along with the simulation time. The RMSF index shows the flexibility of the protein chain concerning a reference frame. The fluctuation of Cα atom coordinates from their average position is the criterion of these effects. RMSF value can be evaluated from the simulation trajectory via Eq. (2) (Bharadwaj et al., 2021).

$$\mathrm{RMSF}_i = \sqrt{\frac{1}{T}\sum_{t=1}^{T}\left(r_i'(t) - r_i(t_{\mathrm{ref}})\right)^2} \ldots \quad (2)$$

In which, T is the trajectory time during the considered time for RMSF calculation, t_{ref} marks as the reference time, r_i defines the position of atom i, regarding the reference time t_{ref} and r_i' represents the position of atom i at time t in residue i after superposition on the reference frame. Figure 3 represents the RMSF plot of Cα for the main protease and complex forms of **4a** and **4b** ligands in three replications.

The observed jumps or peaks in the RMSF plot illustrate the fluctuation of the set of residues is larger than the fluctuation of other residues of the studied complex. RMSF values for the complexes depict large fluctuations in the N- and C-terminus in comparison to other parts of the complexes. This behavior is common and no survey is needed. Regarding 0.15, 0.11 and 0.12 nm as the average RMSF values of MDs 1–3 for **4a** complex, and also 0.11, 0.11 and 0.21 nm for **4b** complex can be concluded that both complexes show almost the same fluctuation during the MD simulation time.

The radius of gyration (Rg) factor is a valuable index to investigate the compactness of the ligand-protein complex during the time of the molecular simulation. This factor estimates the variation of distance between the center of mass of the protein atoms and its terminal. The lower Rg value of the ligand-protein complex indicates higher compactness

Table 4. The docking results of the synthesized compounds.

Compound	Interacting residues	Binding affinity (kcal/mol)
3	MET49, HIS172, GLU166, ASN142, HIS163, LEU141, CYS145	−7.0
4a	GLU290, LEU287, TYR239, LEU272, ASP289, LYS137	−7.6
4b	GLY143, SER144, CYS145, LEU141, GLU166, PRO168, THR190, ALA191	−7.6
4c	ILE249, HIS246, GLU240, PRO241	−7.2
4d	LYS137, LYS5, GLU290, ASP289, ARG131, TYR239	−7.2
4e	LYS137, LEU286, THR199	−7.1
5a	LEU287, ARG131	−7
5b	ARG188, ARG40, CYS85	−6.8
5c	ARG131, THR199, LEU287, LEU286	−6.9
N3(Ref)	LEU287, LEU272, TYR237, ALA193, THR169	−6.4

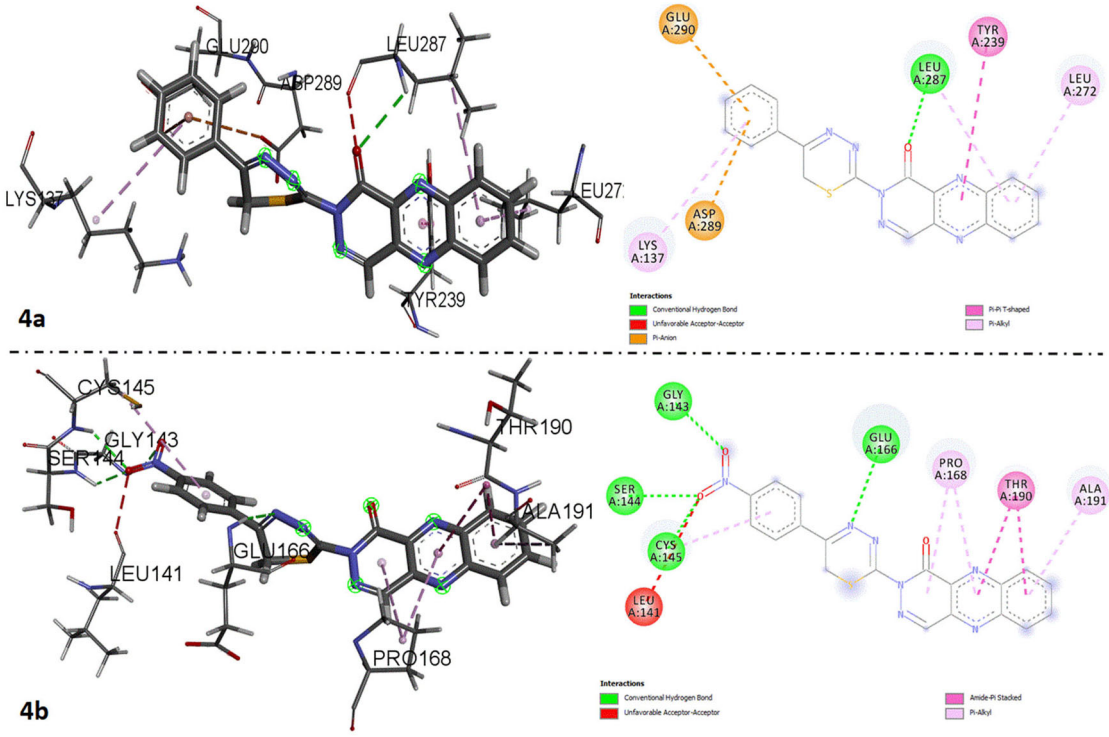

Figure 1. Interacting residues of the best-docked mode for compounds **4a** and **4b**.

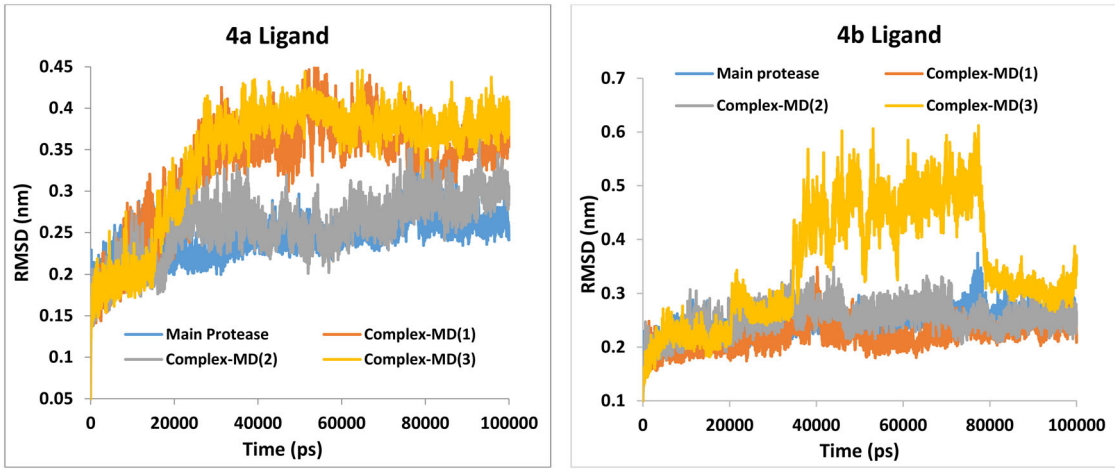

Figure 2. RMSD graph during the time of simulation of the main protease and its complexes with **4a** and **4b**.

and more effective interactions between ligand and protein. Figure 4 illustrates the variation of the Rg value of the ligand–protein complex against the simulation time for three replications. Averaged Rg value of **4a** complex corresponding MDs 1–3 are 2.25, 2.22 and 2.19 nm, respectively. Whereas the obtained results for the **4b** complex are 2.21, 2.2 and 2.21. The mean numbers of Rg value for **4a** and **4b** complexes are 2.22 and 2.20 nm. Averaged Rg value of the main protease during the time of simulation is 2.22 nm. Thus, in reference to the acquired mean values for the complexes,

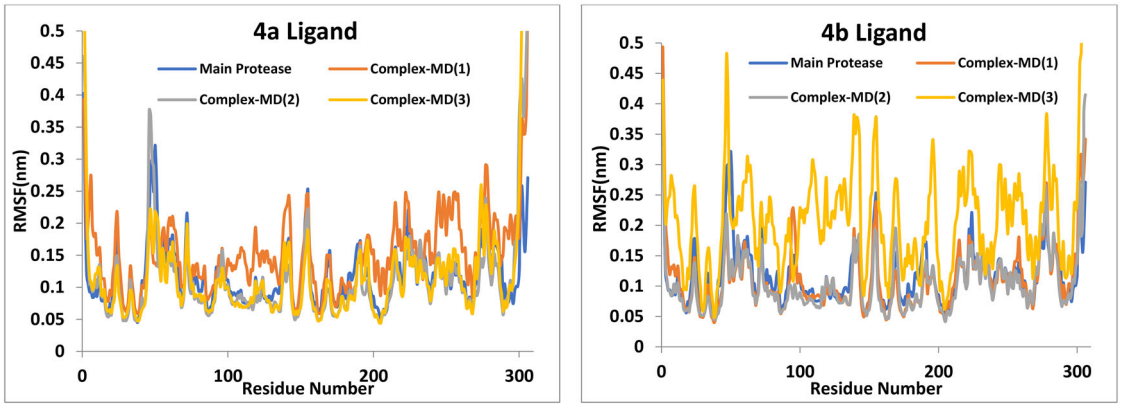

Figure 3. The plots of RMSF (nm) vs. the residue positions for Cα of the main protease and complex forms of **4a** and **4b** ligands.

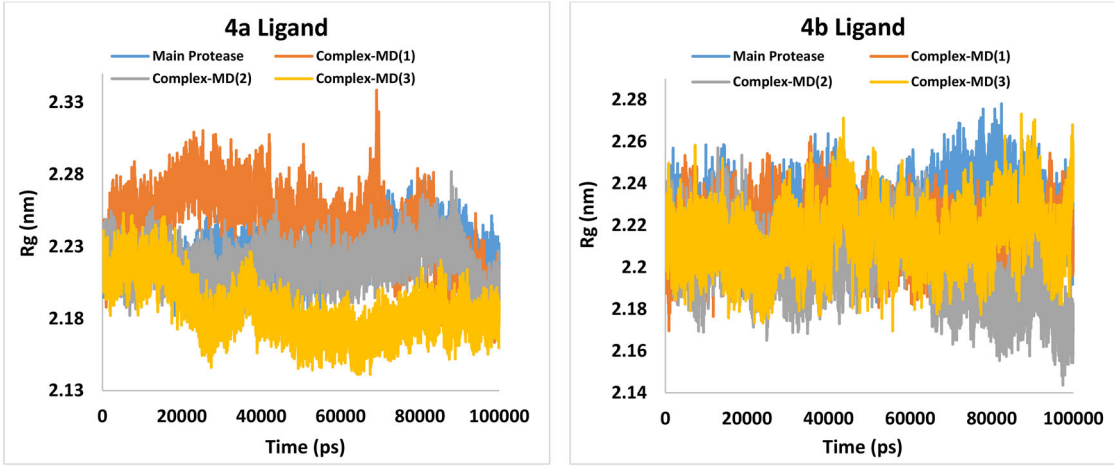

Figure 4. Radius of gyration (Rg) plots of 4a and 4b complexes during 100 ns simulation.

can be concluded that the compactness of the **4b** complex is somewhat more than the **4a** complex.

Figure 5 and Table 5 represent interacting residues of the last pose of the MD simulation. The final snapshots were separated from the respective 100 ns MD trajectories and analyzed for kinds of intermolecular interactions. Van der Waals interactions are dominant ones in the **4a** complex, while, in the **4b** π-interactions possess a significant role in stabilization.

One of determining factors in the binding affinity and stabilization effect of ligands with protein is the number of hydrogen bonds (H-bond). During the whole of 100 ns, the number and distribution of H-bond in the complexes were investigated to specify the stability of the system. It is clear that the average number of H-bond throughout the MD phase has effectively contributed to the consistency of the ligand-protein complex. Figure 6 illustrates the H-bond number plots of **4a** and **4b** complexes. The average value of H-bond numbers for the complexes are 0.89 and 0.56 throughout the 100 ns of simulation, respectively. Thus, it can be concluded that ligand **4a** interacts more effectively with the main protease via hydrogen bonds.

3.4. Binding energy studies

Binding energy investigations were performed using the molecular mechanics Poisson Boltzmann surface area (MM-PBSA) concept in GROMACS that is evaluated via nonbonded interaction energies of the complex. Moreover, this concept is applied to calculate the binding free energy of the enzyme complexes. The collected snapshots at every 1 ps between 80 and 100 ns for all 1–3 replications of MD simulation were used to post-process binding free energies by the g_mmpbsa script (Baker et al., 2001; Kumari et al., 2014) of GROMACS. In the aqueous phase, the binding free energy ΔG (bind, aq) for a non-covalent binding interaction is calculated by Eq. (3)

$$\Delta G(\text{bind, aq}) = \Delta G(\text{bind, vac}) + \Delta G(\text{bind, solv}) \quad (3)$$

In which ΔG (bind, vac) and ΔG(bind, solv) are the binding free energy in vacuum and solvent, respectively. ΔG(bind, solv) is calculated by Eq. (4).

$$\Delta G(\text{bind, solv}) = \Delta G(E:L,\ \text{solv}) - \Delta G(E, \text{solv}) - \Delta G(L, \text{solv}) \quad (4)$$

Here ΔG (E:L, solv), ΔG (E, solv) and ΔG (L, solv) are solvation-free energies of complex, enzyme and ligand, respectively. Generally, the binding interaction of each ligand–enzyme complex is divided into the van der Waals contribution, the electrostatic contribution and the solvation contribution. MMPBSA calculations show that the averaged binding free energy of **4a** and **4b** complexes are −49.05 and −79.43 kJ/mol, respectively. The results of MMPBSA studies

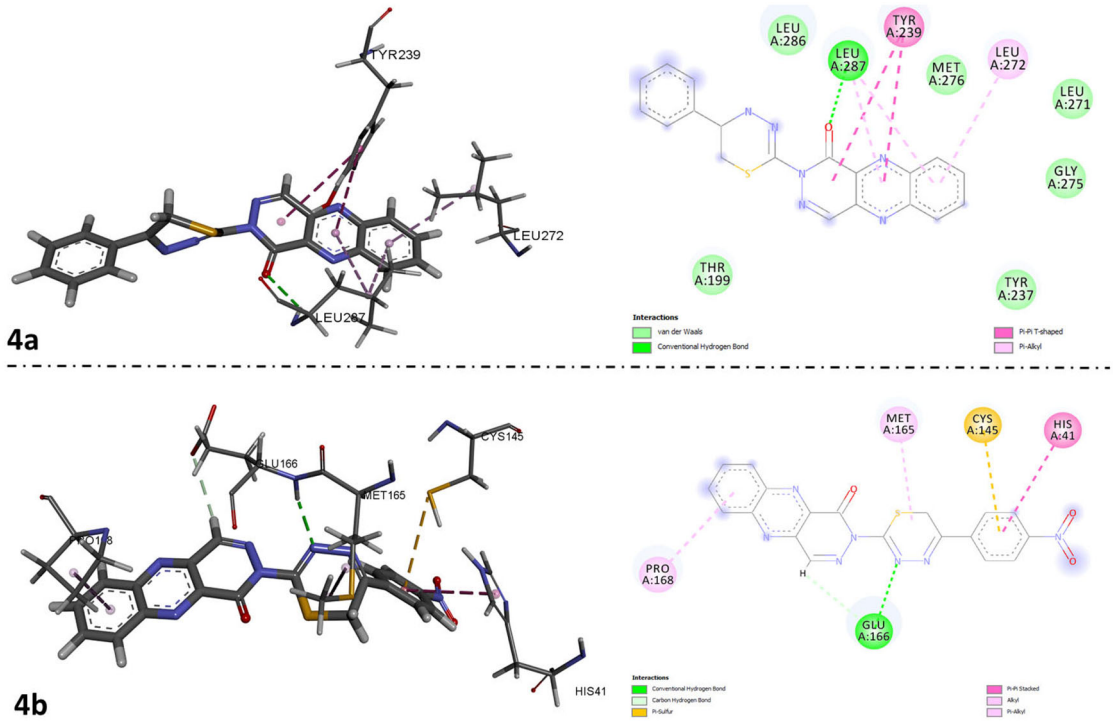

Figure 5. Involved residues of the last pose of MD simulation for complex forms of 4a and 4b ligands.

Table 5. List of involved residues and kind of interactions in the complexation of **4a** and **4b** ligand for the last pose of 100 ns MD trajectory.

4a	LEU286(Van der Waals), LEU287(Hydrogen bond), TYR239(π–π interaction), MET276 (Van der Waals), LEU272(π-alkyl), LEU271(Van der Waals), GLY275(Van der Waals), TYR237(Van der Waals), THR199(Van der Waals)
4b	MET165(alkyl), CYS145(π-sulfur), HIS41(π–π interaction), GLU166(Hydrogen bond), PRO168(π-alkyl)

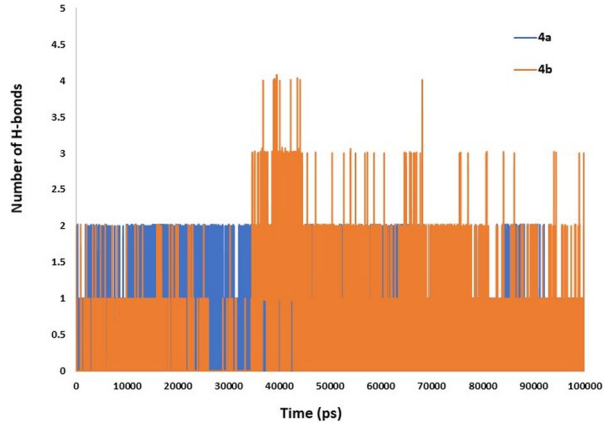

Figure 6. Hydrogen bond (H-bond) plots of 4a and 4b complexes during the 100 ns of simulation.

are presented in Table 6. Van der Waals and polar solvation energies are the most effective factors in the corresponding binding free energies. Regarding the acquired average of the binding free energy can be concluded that the **4b** complex is a more potent inhibitor against the main protease.

4. Conclusion

The COVID-19 pandemic is currently one of the most serious problems and is the leading cause of mortality in many nations worldwide. As a consequence, it is essential to conduct research and develop new therapies for COVID-19. In this study, we aimed to investigate the possibility of pyridazinoquinoxaline derivatives as $3CL^{pro}$ inhibitors. Here, we successfully developed a one-pot manner including the condensation of 2-ethoxycarbonyl-3-formylquinoxaline 1,4-dioxide **1** with thiocarbohydrazide **2**, followed by the reduction of 1,4-di-*N*-oxide to produce 1-oxopyridazino[4,5-*b*]quinoxaline-2(1*H*)-carbothiohydrazide **3**. In fact, by using thiocarbohydrazide as a nucleophile and reducing agent, desired quinoxaline derivative can be afforded through a single-step method. Then, the cyclization reaction of product **3**

Table 6. Calculated polar solvation energy, Van der Waals energy, electrostatic energy and SASA energy components of the total binding energy of (**4a**) and (**4b**) complexes.

Complex	MD Replication	Van der Waals energy (kJ/mol)	Electrostatic energy (kJ/mol)	Polar solvation energy (kJ/mol)	SASA energy (kJ/mol)	Binding energy (kJ/mol)
4a	1st	−55.66	−24.32	44.81	−5.79	−40.96
		± 20.70	± 15.65	± 28.74	± 3.84	± 30.43
	2nd	−81.41	−41.35	83.80	−8.55	−47.51
		± 60.079	± 34.88	± 52.89	± 6.345	± 51.121
	3rd	−73.96	−31.49	54.03	−7.27	−58.69
		± 62.62	± 28.69	± 52.70	± 6.17	± 57.01
	Averaged values	−70.34	−32.39	60.88	−21.61	−49.05
4b	1st	−59.60	−20.64	58.40	−5.80	−27.63
		± 41.08	± 18.72	± 45.21	± 3.99	± 33.84
	2nd	−60.71	−21.56	48.75	−5.69	−39.21
		± 77.86	± 31.23	± 59.15	± 7.31	± 82.87
	3rd	−230.51	−54.40	132.85	−19.37	−171.44
		± 16.85	± 22.18	± 12.82	± 1.02	± 24.96
	Averaged values	−116.94	−32.20	80.00	−10.29	−79.43

with various α-haloketones and triethylorthoesters leads to a new class of pyridazinoquinoxaline derivatives (**4a–e**) and (**5a–c**). Different criteria were provided to distinguish the bioavailability of the prepared molecules, which revealed that the synthesized ligands do not show any toxicity as well as violation of Lipinski's rule of five. Following that, molecular docking and molecular dynamics simulations were performed to scrutinize the inhibitory activity of the synthesized products against the main protease of COVID-19. Based on molecular docking results, compounds **4a** and **4b** exhibited the lowest binding affinity (−7.6 and −7.6 kcal/mol), which represent the favorable orientation in the active site of the chymotrypsin-like cysteine protease ($3CL^{pro}$). In order to gather further information on the ligand–protein interactions, the outcomes of the molecular docking were used as inputs for the molecular dynamics simulation. The MD simulation represented that the averaged binding energy value of **4b** complex is lower than that of **4a** complex, it can be concluded that the inhibitory effects of compound **4b** are more significant than compound **4a**.

5. Experimental section

Melting points (mp) were recorded using an Electrothermal-type 9200 melting point apparatus. The IR spectra were obtained using Avatar 370 FT-IR Thermo Nicolet, and only outstanding absorptions were listed. The ^{1}H NMR (300 MHz) and ^{13}C NMR (75 MHz) spectra were recorded using a Bruker Avance DRX-300 Fourier transformer spectrometer. Chemical shifts were reported in ppm downfield from tetramethylsilane (TMS) as an internal standard. The mass spectra were scanned using Varian Mat CH-7 at 70 eV.

5.1. 1-Oxopyridazino[4,5-b]quinoxaline-2(1H)-carbothiohydrazide (3)

A mixture of 2-ethoxycarbonyl-3-formylquinoxaline 1,4-dioxide (**1**) (5 mmol, 1.31 gr) and thiocarbohydrazide (**2**) (5 mmol, 0.53 gr) in ethanol was refluxed for 8 h. After completing the reaction, the solvent was evaporated under reduced pressure. The crude product was recrystallized from aqueous dimethylformamide. Yellow solid (0.92 g, 68%); mp 211–213 °C. ^{1}H NMR (300 MHz, DMSO-d_6) δ 8.73 (s, 1H, CH-N of oxopyridazine), 8.47 (s, 1H, NH), 7.95–8.02 (m, 4H, Ar), 3.07 (s, 2H, NH_2). ^{13}C NMR (75 MHz, DMSO-d_6) δ 168.8, 164.3, 151.9, 144.5, 143.5, 143.3, 139.8, 139.3, 138.9, 125.8, 125.6. IR (KBr disc, cm^{-1}) 3378, 3207, 3080, 2990, 1690, 1337. MS (*m/z*) 272 (M^+). Anal. calcd for $C_{11}H_8N_6OS$: C, 48.52; H, 2.96; N, 30.87; S, 11.77. Found: C, 48.70; H, 2.91; N, 30.72; S, 11.57.

5.2. Synthesis of compounds 4a–e; general procedure

To 1-Oxopyridazino[4,5-*b*]quinoxaline-2(1*H*)-carbothiohydrazide (**3**) (1 mmol, 0.272 gr) in ethanol was added appropriate α-haloketones (1 mmol), and the mixture was refluxed for 2 h. The solvent was evaporated under reduced pressure, and the precipitate was recrystallized from aqueous dimethylformamide.

5.2.1. 2-(5-Phenyl-6H-1,3,4-thiadiazin-2-yl)pyridazino[4,5-b]quinoxalin-1(2H)-one (4a)

Orange solid (0.25 g, 67%); mp 236–239 °C. ^{1}H NMR (300 MHz, DMSO-d_6) δ 8.76 (s, 1H, CH-N), 8.46–8.49 (m, 2H, Ar), 8.00–8.03 (m, 2H, Ar), 7.87–7.90 (m, 2H, Ar), 7.50–7.53 (m, 3H, Ar), 4.10 (s, 2H, CH_2). ^{13}C NMR (75 MHz, DMSO-d_6) δ 172.3, 164.7, 160.2, 159.4, 153.5, 141.6, 138.1, 137.1, 133.4, 132.9, 130.5, 129.2, 126.6, 120.3, 114.8, 114.0, 23.2. IR (KBr disc, cm^{-1}) 3043, 2967, 1680, 1610. MS (*m/z*) 374 (M^+). Anal. Calcd for $C_{19}H_{12}N_6OS$: C, 61.28; H, 3.25; N, 22.57; S, 8.61. Found: C, 61.13; H, 3.19; N, 22.34; S, 8.35.

5.2.2. 2-(5-(4-Nitrophenyl)-6H-1,3,4-thiadiazin-2-yl)pyridazino[4,5-b]quinoxalin-1(2H)-one (4b)

Red solid (0.29 g,71%); mp 220–222 °C. ^{1}H NMR (300 MHz, DMSO-d_6) δ 8.72 (s, 1H, CH-N), 8.25–8.32 (m, 4H, Ar-H), 7.91–7.96 (m, 4H, Ar-H), 4.13 (s, 2H, CH_2). ^{13}C NMR (75 MHz, DMSO-d_6) δ 172.3, 159.4, 159.2, 148.3, 147.6, 139.9, 138.9, 138.0, 137.2, 136.4, 136.0, 133.4, 132.8, 130.3, 127.7, 124.4, 123.7, 120.3, 30.0. IR (KBr disc, cm^{-1}) 3091, 2981, 1690, 1597. MS (*m/z*) 417. Anal. Calcd for $C_{19}H_{11}N_7O_3S$: C, 54.67; H, 2.66; N, 23.49; S, 7.68. Found: C, 54.86; H, 2.53; N, 23.72; S, 7.53.

5.2.3. 2-(5-(4-Bromophenyl)-6H-1,3,4-thiadiazin-2-yl)pyridazino[4,5-b]quinoxalin-1(2H)-one (4c)

Orange solid (0.28 g, 64%); mp 230–232 °C. ^{1}H NMR (300 MHz, DMSO-d_6) δ 8.60 (s, 1H, CH-N), 7.93–7.99 (m, 2H, Ar-H), 7.78–7.85 (m, 6H, Ar-H), 4.01 (s, 2H, CH_2). ^{13}C NMR (75 MHz, DMSO-d_6) δ 170.1, 164.0, 163.8, 152.9, 152.2, 144.5, 143.5, 142.6, 141.8, 141.0, 140.6, 138.0, 137.4, 134.9, 132.3, 129.0, 128.3, 124.9, 24.3. IR (KBr disc, cm^{-1}) 3096, 3043, 2967, 1685, 1598. MS (*m/z*) 451. Anal. Calcd for $C_{19}H_{11}BrN_6OS$: C, 50.57; H, 2.46; N, 18.62; S, 7.10. Found: C, 50.30; H, 2.35; N, 18.44; S, 7.36.

5.2.4. 2-(5-(4-Methoxyphenyl)-6H-1,3,4-thiadiazin-2-yl)pyridazino[4,5-b]quinoxalin-1(2H)-one (4d)

Green solid (0.29 g, 73%); mp 209–211 °C. ^{1}H NMR (300 MHz, DMSO-d_6) δ 8.73 (s, 1H, CH-N), 7.92–8.02 (m, 4H, Ar-H), 7.59–7.62 (m, 2H, Ar-H), 7.02–7.07 (m, 2H, Ar-H), 4.05 (s, 2H, CH_2), 3.82 (s, 3H, CH_3). ^{13}C NMR (75 MHz, DMSO-d_6) δ 172.3, 164.7, 160.2, 159.4, 153.5, 141.8, 137.9, 137.8, 136.6, 133.5, 132.4, 130.7, 128.3, 122.6, 120.2, 114.7, 114.0, 55.7, 22.2. IR (KBr disc, cm^{-1}) 3101, 2973, 2900, 1690, 1610. MS (*m/z*) 402. Anal. Calcd for $C_{20}H_{14}N_6O_2S$: C, 59.69; H, 3.51; N, 20.88; S, 7.97. Found: C, 59.53; H, 3.47; N, 21.17; S, 7.88.

5.2.5. 2-(5-(p-tolyl)-6H-1,3,4-thiadiazin-2-yl)pyridazino[4,5-b]quinoxalin-1(2H)-one (4e)

Green solid (0.25 g, 65%); mp 216–218 °C. ^{1}H NMR (300 MHz, DMSO-d_6) δ 8.61 (s, 1H, CH-N), 7.85–7.91 (m, 4H, Ar-H), 7.72–7.75 (m, 2H, Ar-H), 7.35–7.36 (m, 2H, Ar-H), 3.95 (s, 2H, CH_2), 2.39 (s, 3H, CH_3). ^{13}C NMR (75 MHz, DMSO-d_6) δ 172.3, 164.7, 160.2, 159.4, 153.5, 141.8, 137.9, 137.8, 136.6, 136.2, 133.5, 132.8, 132.4, 130.7, 128.3, 122.6, 120.2, 22.2, 19.6. IR (KBr disc, cm^{-1}) 3090, 2973, 2925, 1691, 1597. MS (*m/z*) 386. Anal. Calcd for $C_{20}H_{14}N_6OS$: C, 62.16; H, 3.65; N, 21.75; S, 8.30. Found: C, 62.35; H, 3.58; N, 21.65; S, 8.38.

5.3. General procedure for the synthesis of 5a–c

A mixture of 1-Oxopyridazino[4,5-*b*]quinoxaline-2(1*H*)-carbothiohydrazide (**3**) (1 mmol, 0.272 gr) and triethylorthoformate/acetate/propionate (2 mmol) in glacial acetic acid (1 mL) was heated under reflux condition for 4 h. The progress of the reaction was monitored by TLC using chloroform:methanol (30:1). After the completion of the reaction, the solvent was evaporated under reduced pressure, then water (5 mL) was added, and the resulting precipitate was filtered off. The residue was recrystallized in aqueous dimethylformamide to afford the desired product.

5.3.1. 2-(1,3,4-Thiadiazol-2-yl)pyridazino[4,5-b]quinoxalin-1(2H)-one (5a)

Yellow solid (0.17 g, 61%); mp 204–207 °C. ^{1}H NMR (300 MHz, DMSO-d_6) δ 9.10 (s, 1H, CH-N), 8.80 (s, 1H, thiadiazol), 8.26–8.31 (m, 2H, Ar-H), 7.85–7.89 (m, 2H, Ar-H). ^{13}C NMR (75 MHz, DMSO-d_6) δ 163.6, 159.1, 146.7, 139.3, 138.2, 138.1, 134.5, 134.0, 133.7, 133.1, 120.6, 120.4. IR (KBr disc, cm^{-1}) 3112, 2970, 1692, 1610. MS (*m/z*) 282. Anal. Calcd for $C_{12}H_6N_6OS$: C, 51.06; H, 2.14; N, 29.77; S, 11.36. Found: C, 50.86; H, 2.07; N, 29.50; S, 11.28.

5.3.2. 2-(5-Methyl-1,3,4-thiadiazol-2-yl)pyridazino[4,5-b]quinoxalin-1(2H)-one (5b)

Yellow solid (0.18 g, 64%); mp 247–249 °C. ^{1}H NMR (300 MHz, DMSO-d_6) δ 9.16 (s, 1H, CH-N), 8.43–8.50 (m, 2H, Ar-H), 8.01–8.08 (m, 2H, Ar-H), 2.28 (s, 3H, CH_3). ^{13}C NMR (75 MHz, DMSO-d_6) δ 164.7, 160.2, 147.8, 140.4, 139.3, 139.2, 135.6, 135.1, 134.8, 134.2, 121.7, 121.5, 19.2. IR (KBr disc, cm^{-1}) 3088, 2958, 1685, 1605. MS (*m/z*) 296. Anal. Calcd for $C_{13}H_8N_6OS$: C, 52.70; H, 2.72; N, 28.36; S, 10.82. Found: C, 52.51; H, 2.67; N, 28.13; S, 10.68.

5.3.3. 2-(5-Ethyl-1,3,4-thiadiazol-2-yl)pyridazino[4,5-b]quinoxalin-1(2H)-one (5c)

Yellow solid (0.21 g, 70%); mp 231–234 °C. ^{1}H NMR (300 MHz, DMSO-d_6) δ 9.17 (s, 1H, CH-N), 8.44–8.49 (m, 2H, Ar-H), 8.03–8.06 (m, 2H, Ar-H), 2.65 (q, $J = 7.5$ Hz, 2H, CH_2 of Et), 1.38 (t, $J = 7.5$ Hz, 3H, CH_3 of Et). ^{13}C NMR (75 MHz, DMSO-d_6) δ 164.4, 159.9, 147.6, 140.1, 139.1, 139.0, 135.4, 134.9, 134.6, 134.0, 121.5, 121.3, 23.2, 15.0. IR (KBr disc, cm^{-1}) 3112, 2918, 1690, 1598. MS (*m/z*) 310. Anal. Calcd for $C_{14}H_{10}N_6OS$: C, 54.18; H, 3.25; N, 27.08; S, 10.33. Found: C, 53.92; H, 3.16; N, 26.93; S, 10.40.

Disclosure statement

No potential conflict of interest was reported by the author(s).

Funding

The authors gratefully acknowledge the Research Council of Ferdowsi University of Mashhad for financial support of this Project (3/54936).

References

Abouzid, K. A., Khalil, N. A., Ahmed, E. M., El-Latif, H. A. A., & El-Araby, M. E. (2010). Structure-based molecular design, synthesis, and in vivo anti-inflammatory activity of pyridazinone derivatives as nonclassic COX-2 inhibitors. *Medicinal Chemistry Research*, *19*(7), 629–642. https://doi.org/10.1007/s00044-009-9218-4

Abraham, M. J., Murtola, T., Schulz, R., Páll, S., Smith, J. C., Hess, B., & Lindahl, E. (2015). GROMACS: High performance molecular simulations through multi-level parallelism from laptops to supercomputers. *SoftwareX*, *1*, 19–25.

Asif, M. (2015). Overview on Emorfazone and other related 3 (2H) pyridazinone analogues displaying analgesic and anti-Inflammatory activity.

Assis, L. C., de Castro, A. A., de Jesus, J., Nepovimova, E., Kuca, K., Ramalho, T. C., & La Porta, F. A. (2021). Computational evidence for nitro derivatives of quinoline and quinoline N-oxide as low-cost alternative for the treatment of SARS-CoV-2 infection. *Scientific Reports*, *11*(1), 1–11. https://doi.org/10.1038/s41598-021-85280-9

Avcı, D., Bahçeli, S., Tamer, Ö., & Atalay, Y. (2015). Comparative study of DFT/B3LYP, B3PW91, and HSEH1PBE methods applied to molecular structures and spectroscopic and electronic properties of flufenpyr and amipizone. *Canadian Journal of Chemistry*, *93*(10), 1147–1156. https://doi.org/10.1139/cjc-2015-0176

Baker, N. A., Sept, D., Joseph, S., Holst, M. J., & McCammon, J. A. (2001). Electrostatics of nanosystems: Application to microtubules and the

ribosome. *Proceedings of the National Academy of Sciences of United States of America*, *98*(18), 10037–10041. https://doi.org/10.1073/pnas.181342398

Bansal, R., Kumar, D., Carron, R., & de la Calle, C. (2009). Synthesis and vasodilatory activity of some amide derivatives of 6-(4-carboxymethyloxyphenyl)-4,5-dihydro-3(2H)-pyridazinone. *European Journal of Medicinal Chemistry*, *44*(11), 4441–4447. https://doi.org/10.1016/j.ejmech.2009.06.006

Barriga-González, G., Aliaga, C., Chamorro, E., Olea-Azar, C., Norambuena, E., Porcal, W., González, M., & Cerecetto, H. (2020). Synthesis and evaluation of new heteroaryl nitrones with spin trap properties. *RSC Advances*, *10*(66), 40127–40135. https://doi.org/10.1039/D0RA07720H

Berendsen, H. J., Postma, J. P., van Gunsteren, W. F., & Hermans, J. (1981). Interaction models for water in relation to protein hydration. In *Intermolecular forces* (pp. 331–342). Springer.

Bharadwaj, S., Dubey, A., Yadava, U., Mishra, S. K., Kang, S. G., & Dwivedi, V. D. (2021). Exploration of natural compounds with anti-SARS-CoV-2 activity via inhibition of SARS-CoV-2 Mpro. *Briefings in Bioinformatics*, *22*(2), 1361–1377. https://doi.org/10.1093/bib/bbaa382

Bigonah-Rasti, S., Sheikhi-Mohammareh, S., Saadat, K., & Shiri, A. (2020). Novel tricyclic 2-alkoxy-8-methyl-6-(pyrrolidin-1-yl)-4 H-[1, 2, 4] triazolo [5, 1-f] purine derivatives: Synthesis and Characterization. *polycyclic Aromatic Compounds*, *42*(5), 2644–2654.

Bofill, J. M. (1995). A conjugate gradient algorithm with a trust region for molecular geometry optimization. *Molecular Modeling Annual*, *1*(1), 11–17. https://doi.org/10.1007/s008940050002

Brogi, S., Ramalho, T. C., Kuca, K., Medina-Franco, J. L., & Valko, M. (2020). In silico methods for drug design and discovery. *Frontiers in Chemistry*, *8*, 612. https://doi.org/10.3389/fchem.2020.00612

Bussi, G., Donadio, D., & Parrinello, M. (2007). Canonical sampling through velocity rescaling. *The Journal of Chemical Physics*, *126*(1), 014101. https://doi.org/10.1063/1.2408420

Chemboli, R., Kapavarapu, R., Deepti, K., Prasad, K., Reddy, A. G., Kumar, A. N., Rao, M. V. B., & Pal, M. (2021). Pyrrolo [2, 3-b] quinoxalines in attenuating cytokine storm in COVID-19: Their sonochemical synthesis and in silico/in vitro assessment. *Journal of Molecular Structure*, *1230*, 129868. https://doi.org/10.1016/j.molstruc.2020.129868

Dai, W., Zhang, B., Jiang, X.-M., Su, H., Li, J., Zhao, Y., Xie, X., Jin, Z., Peng, J., & Liu, F. (2020). Structure-based design, synthesis and biological evaluation of peptidomimetic aldehydes as a novel series of antiviral drug candidates targeting the SARS-CoV-2 main protease. *BioRxiv*, *368*, 1331–1335.

Daina, A., Michielin, O., & Zoete, V. (2017). SwissADME: a free web tool to evaluate pharmacokinetics, drug-likeness and medicinal chemistry friendliness of small molecules. *Scientific Reports*, *7*(1), 1–13. https://doi.org/10.1038/srep42717

de Lucio, H., García-Marín, J., Sánchez-Alonso, P., García-Soriano, J. C., Toro, M. Á., Vaquero, J. J., Gago, F., Alajarín, R., & Jiménez-Ruiz, A. (2022). Pyridazino-pyrrolo-quinoxalinium salts as highly potent and selective leishmanicidal agents targeting trypanothione reductase. *European Journal of Medicinal Chemistry*, *227*, 113915. https://doi.org/10.1016/j.ejmech.2021.113915

Diallo, B., Swart, T., Hoppe, H. C., Tastan Bishop, Ö., & Lobb, K. (2021). Potential repurposing of four FDA approved compounds with anti-plasmodial activity identified through proteome scale computational drug discovery and in vitro assay. *Scientific Reports*, *11*(1), 1–15. https://doi.org/10.1038/s41598-020-80722-2

discovery-studio-visualizer-download. https://discover.3ds.com/discovery-studio-visualizer-download.

Divya, K., Savitha, D., Krishna, G. A., Dhanya, T., & Mohanan, P. (2022). Crystal structure, DFT studies, Hirshfeld surface and energy framework analysis of 4-(5-nitro-thiophen-2-yl)-pyrrolo [1, 2-a] quinoxaline: A potential SARS-CoV-2 main protease inhibitor. *Journal of Molecular Structure*, *1251*, 131932. https://doi.org/10.1016/j.molstruc.2021.131932

Dolatkhah, Z., Javanshir, S., Sadr, A. S., Hosseini, J., & Sardari, S. (2017). Synthesis, molecular docking, molecular dynamics studies, and biological evaluation of 4 h-chromone-1, 2, 3, 4-tetrahydropyrimidine-5-carboxylate derivatives as potential antileukemic agents. *Journal of Chemical Information and Modeling*, *57*(6), 1246–1257. https://doi.org/10.1021/acs.jcim.6b00138

El Bakri, Y., Anouar, E. H., Ahmad, S., Nassar, A. A., Taha, M. L., Mague, J. T., El Ghayati, L., & Essassi, E. M. (2021). Synthesis and identification of novel potential molecules against COVID-19 main protease through structure-guided virtual screening approach. *Applied Biochemistry and Biotechnology*, *193*(11), 3602–3623. https://doi.org/10.1007/s12010-021-03615-8

Elmore, D. E., & Dougherty, D. A. (2001). Molecular dynamics simulations of wild-type and mutant forms of the Mycobacterium tuberculosis MscL channel. *Biophysical Journal*, *81*(3), 1345–1359. https://doi.org/10.1016/S0006-3495(01)75791-8

El-Tombary, A. A., & El-Hawash, S. A. M. (2014). Synthesis, antioxidant, anticancer and antiviral activities of novel quinoxaline hydrazone derivatives and their acyclic C-nucleosides. *Medicinal Chemistry*, *10*(5), 521–532. https://doi.org/10.2174/1573406411309660069

Fabian, L., Porro, M. T., Gomez, N., Salvatori, M., Turk, G., Estrin, D., & Moglioni, A. (2020). Design, synthesis and biological evaluation of quinoxaline compounds as anti-HIV agents targeting reverse transcriptase enzyme. *European Journal of Medicinal Chemistry*, *188*, 111987. https://doi.org/10.1016/j.ejmech.2019.111987

Frisch, M., Trucks, G., Schlegel, H., Scuseria, G., Robb, M., Cheeseman, J., Scalmani, G., Barone, V., Mennucci, B., & Petersson, G. (2009). *Gaussian 09, Revision D. 01*. Gaussian, Inc. http://www.gaussian.com.

Gentile, D., Patamia, V., Scala, A., Sciortino, M. T., Piperno, A., & Rescifina, A. (2020). Putative inhibitors of SARS-CoV-2 main protease from a library of marine natural products: A virtual screening and molecular modeling study. *Marine Drugs*, *18*(4), 225. https://doi.org/10.3390/md18040225

Guillon, J., Cohen, A., Gueddouda, N. M., Das, R. N., Moreau, S., Ronga, L., Savrimoutou, S., Basmaciyan, L., Monnier, A., Monget, M., Rubio, S., Garnerin, T., Azas, N., Mergny, J.-L., Mullié, C., & Sonnet, P. (2017). Design, synthesis and antimalarial activity of novel bis {N-[(pyrrolo [1, 2-a] quinoxalin-4-yl) benzyl]-3-aminopropyl} amine derivatives. *Journal of Enzyme Inhibition and Medicinal Chemistry*, *32*(1), 547–563.

Isa, M. A., Mustapha, A., Qazi, S., Raza, K., Allamin, I. A., Ibrahim, M. M., & Mohammed, M. M. (2020). In silico molecular docking and molecular dynamic simulation of potential inhibitors of 3C-like main proteinase (3CLpro) from severe acute respiratory syndrome coronavirus-2 (SARS-CoV-2) using selected african medicinal plants. *Advances in Traditional Medicine*, *53*(7), 1– 17. https://doi.org/10.1007/s13596-020-00523-w.

Jaso, A., Zarranz, B., Aldana, I., & Monge, A. (2005). Synthesis of new quinoxaline-2-carboxylate 1, 4-dioxide derivatives as anti-mycobacterium t uberculosis agents. *Journal of Medicinal Chemistry*, *48*(6), 2019–2025. https://doi.org/10.1021/jm049952w

Jilloju, P. C., Persoons, L., Kurapati, S. K., Schols, D., De Jonghe, S., Daelemans, D., & Vedula, R. R. (2022). Discovery of (±)-3-(1 H-pyrazol-1-yl)-6, 7-dihydro-5 H-[1, 2, 4] triazolo [3, 4-b][1, 3, 4] thiadiazine derivatives with promising in vitro anticoronavirus and antitumoral activity. *Molecular Diversity*, *26*(3), 1357–1371. https://doi.org/10.1007/s11030-021-10258-8

Jin, Z., Du, X., Xu, Y., Deng, Y., Liu, M., Zhao, Y., Zhang, B., Li, X., Zhang, L., Peng, C., Duan, Y., Yu, J., Wang, L., Yang, K., Liu, F., Jiang, R., Yang, X., You, T., Liu, X., … Yang, H. (2020). Structure of M. sup. pro from SARS-CoV-2 and discovery of its inhibitors. *Nature*, *582*(7811), 289–293. https://doi.org/10.1038/s41586-020-2223-y

Keivanloo, A., Abbaspour, S., Sepehri, S., & Bakherad, M. (2020). Synthesis, antibacterial activity and molecular docking study of a series of 1, 3-oxazole-quinoxaline amine hybrids. *Polycyclic Aromatic Compounds*, *42*(5), 2378–2391.

Kohandel, O., Sheikhi-Mohammareh, S., Oroojalian, F., Memariani, T., Mague, J., & Shiri, A. (2021). A Dimroth rearrangement approach for the synthesis of selenopheno [2, 3-e][1, 2, 4] triazolo [1, 5-c] pyrimidines with cytotoxic activity on breast cancer cells. *Molecular Diversity*, *26*(3), 1621–1633.

Kumari, R., Kumar, R., Consortium, O. S. D. D., & Lynn, A. (2014). g_mmpbsa—A GROMACS tool for high-throughput MM-PBSA calculations. *Journal of Chemical Information and Modeling*, *54*(7), 1951–1962. https://doi.org/10.1021/ci500020m

Kurasawa, Y., Kawase, A., Takizawa, J., Maesaki, Y., Kaji, E., Okamoto, Y., & Kim, H. S. (2005). Quinolone analogues 8 [1-6]. Synthesis of 3-

aminopyridazino-[3, 4-b] quinoxalin-4 (lH)-one. *Journal of Heterocyclic Chemistry*, *42*(4), 551–556. https://doi.org/10.1002/jhet.5570420412

Kurasawa, Y., & Kim, H. S. (2002). Synthesis and biological activities of quinolone analogues: Pyridazino [3, 4-b] quinoxalin-4-one. *Journal of Heterocyclic Chemistry*, *39*(3), 551–570. https://doi.org/10.1002/jhet.5570390311

Kurasawa, Y., Nakamura, M., Ashida, H., Masuda, M., Kaji, E., Okamoto, Y., & Kim, H. S. (2007). Quinolone analogues 9. Synthesis of 7-methylsulfanyl-and 7-methanesulfonylpyridazino [3, 4-b] quinoxalin-4 (1H)-ones. *Journal of Heterocyclic Chemistry*, *44*(6), 1231–1234. https://doi.org/10.1002/jhet.5570440602

Li, W., Li, X., De Clercq, E., Zhan, P., & Liu, X. (2015). Discovery of potent HIV-1 non-nucleoside reverse transcriptase inhibitors from arylthioacetanilide structural motif. *European Journal of Medicinal Chemistry*, *102*, 167–179. https://doi.org/10.1016/j.ejmech.2015.07.043

Lima, L. M., Vicente, E., Solano, B., Pérez-Silanes, S., Aldana, I., & Monge, A. (2008). Unexpected reduction of ethyl 3-phenylquinoxaline-2-carboxylate 1, 4-Di-N-oxide derivatives by amines. *Molecules (Basel, Switzerland)*, *13*(1), 78–85. https://doi.org/10.3390/molecules13010078

Liu, P., Liu, H., Sun, Q., Liang, H., Li, C., Deng, X., Liu, Y., & Lai, L. (2020). Potent inhibitors of SARS-CoV-2 3C-like protease derived from N-substituted isatin compounds. *European Journal of Medicinal Chemistry*, *206*, 112702. https://doi.org/10.1016/j.ejmech.2020.112702

Llanes, A., Cruz, H., Nguyen, V. D., Larionov, O. V., & Fernández, P. L. (2020). A computational approach to explore the interaction of semi-synthetic nitrogenous heterocyclic compounds with the SARS-CoV-2 main protease. *Biomolecules*, *11*(1), 18. https://doi.org/10.3390/biom11010018

Malinka, W., Redzicka, A., & Lozach, O. (2004). New derivatives of pyrrolo [3, 4-d] pyridazinone and their anticancer effects. *Farmaco (Societa Chimica Italiana : 1989)*, *59*(6), 457–462. https://doi.org/10.1016/j.farmac.2004.03.002

Moghimi, P., Sabet-Sarvestani, H., Kohandel, O., & Shiri, A. (2022). Pyrido [1, 2-e] purine: Design and synthesis of appropriate inhibitory candidates against the main protease of COVID-19. *The Journal of Organic Chemistry*, *87*(6), 3922–3933. https://doi.org/10.1021/acs.joc.1c02237

Monge, A., Palop, J., González, M., Martínez-Crespo, F., De Ceráin, A. L., Sáinz, Y., Narro, S., Barker, A., & Hamilton, E. (1995). New hypoxia-selective cytotoxines derived from quinoxaline 1, 4-dioxides. *Journal of Heterocyclic Chemistry*, *32*(4), 1213–1217. https://doi.org/10.1002/jhet.5570320420

Montana, M., Mathias, F., Terme, T., & Vanelle, P. (2019). Antitumoral activity of quinoxaline derivatives: A systematic review. *European Journal of Medicinal Chemistry*, *163*, 136–147. https://doi.org/10.1016/j.ejmech.2018.11.059

Nageswara Rao, D., Zephyr, J., Henes, M., Chan, E. T., Matthew, A. N., Hedger, A. K., Conway, H. L., Saeed, M., Newton, A., Petropoulos, C. J., Huang, W., Kurt Yilmaz, N., Schiffer, C. A., & Ali, A. (2021). Discovery of quinoxaline-based P1–P3 macrocyclic NS3/4A protease inhibitors with potent activity against drug-resistant hepatitis C virus variants. *Journal of Medicinal Chemistry*, *64*(16), 11972–11989. https://doi.org/10.1021/acs.jmedchem.1c00554

Padilla-Salinas, R., Sun, L., Anderson, R., Yang, X., Zhang, S., Chen, Z. J., & Yin, H. (2020). Discovery of small-molecule cyclic GMP-AMP synthase inhibitors. *The Journal of Organic Chemistry*, *85*(3), 1579–1600. https://doi.org/10.1021/acs.joc.9b02666

Parrinello, M., & Rahman, A. (1981). Polymorphic transitions in single crystals: A new molecular dynamics method. *Journal of Applied Physics*, *52*(12), 7182–7190. https://doi.org/10.1063/1.328693

Petrou, A., Zagaliotis, P., Theodoroula, N. F., Mystridis, G. A., Vizirianakis, I. S., Walsh, T. J., & Geronikaki, A. (2022). Thiazole/thiadiazole/benzothiazole based thiazolidin-4-one derivatives as potential inhibitors of main protease of SARS-CoV-2. *Molecules*, *27*(7), 2180. https://doi.org/10.3390/molecules27072180

Petrova, S. S., & Solov'ev, A. D. (1997). The origin of the method of steepest descent. *Historia Mathematica*, *24*(4), 361–375. https://doi.org/10.1006/hmat.1996.2146

Pettersen, E. F., Goddard, T. D., Huang, C. C., Couch, G. S., Greenblatt, D. M., Meng, E. C., & Ferrin, T. E. (2004). UCSF Chimera—a visualization system for exploratory research and analysis. *Journal of Computational Chemistry*, *25*(13), 1605–1612. https://doi.org/10.1002/jcc.20084

Sheikhi-Mohammareh, S., & Shiri, A. (2018). An alternative regioselective approach for the synthesis of highly functionalized derivatives of pyrazolo [5, 1-b] purine scaffold. *Journal of Heterocyclic Chemistry*, *55*(9), 2055–2060. https://doi.org/10.1002/jhet.3242

Sheikhi-Mohammareh, S., Shiri, A., Maleki, E. H., Matin, M. M., Beyzaei, H., Baranipour, P., Oroojalian, F., & Memariani, T. (2020). Synthesis of various derivatives of [1, 3] selenazolo [4, 5-d] pyrimidine and exploitation of these heterocyclic systems as antibacterial, antifungal, and anticancer agents. *ChemistrySelect*, *5*(32), 10060–10066. https://doi.org/10.1002/slct.202002474

Sherif, E.-S M., & Ahmed, A. H. (2010). Synthesizing new hydrazone derivatives and studying their effects on the inhibition of copper corrosion in sodium chloride solutions. *Synthesis and Reactivity in Inorganic, Metal-Organic, and Nano-Metal Chemistry*, *40*(6), 365–372. https://doi.org/10.1080/15533174.2010.492546

Silva Arouche, T. d., Reis, A. F., Martins, A. Y., S., Costa, J. F., Carvalho Junior, R. N., J. C., & Neto, A. M. (2020). Interactions between remdesivir, ribavirin, favipiravir, galidesivir, hydroxychloroquine and chloroquine with fragment molecular of the COVID-19 main protease with inhibitor N3 complex (PDB ID: 6LU7) using molecular docking. *Journal of Nanoscience and Nanotechnology*, *20*(12), 7311–7323.

Sosnovskikh, V. Y., Safrygin, A. V., Irgashev, R. A., Ezhikova, M. A., & Kodess, M. I. (2016). Synthesis of 4-arylamino-3-(trifluoromethyl) pyridazines and pyridazino [3, 4-b] quinoxalines (as by-products) from 3-aroylmethyl-2-(trifluoromethyl) quinoxalines and hydrazine hydrate. *RSC Advances*, *6*(36), 30056–30069. https://doi.org/10.1039/C5RA27032D

Sun, L., Huang, T., Dick, A., Meuser, M. E., Zalloum, W. A., Chen, C.-H., Ding, X., Gao, P., Cocklin, S., Lee, K.-H., Zhan, P., & Liu, X. (2020). Design, synthesis and structure-activity relationships of 4-phenyl-1H-1, 2, 3-triazole phenylalanine derivatives as novel HIV-1 capsid inhibitors with promising antiviral activities. *European Journal of Medicinal Chemistry*, *190*, 112085. https://doi.org/10.1016/j.ejmech.2020.112085

Thota, S., & Bansal, R. (2010). Synthesis of new pyridazinone derivatives as platelet aggregation inhibitors. *Medicinal Chemistry Research*, *19*(8), 808–816. https://doi.org/10.1007/s00044-009-9232-6

Ton, A. T., Gentile, F., Hsing, M., Ban, F., & Cherkasov, A. (2020). Rapid identification of potential inhibitors of SARS-CoV-2 main protease by deep docking of 1.3 billion compounds. *Molecular Informatics*, *39*(8), 2000028. https://doi.org/10.1002/minf.202000028

Trott, O., & Olson, A. J. (2010). AutoDock Vina: Improving the speed and accuracy of docking with a new scoring function, efficient optimization, and multithreading. *Journal of Computational Chemistry*, *31*(2), 455–461. https://doi.org/10.1002/jcc.21334

Tseng, C.-H., Chen, Y.-R., Tzeng, C.-C., Liu, W., Chou, C.-K., Chiu, C.-C., & Chen, Y.-L. (2016). Discovery of indeno [1, 2-b] quinoxaline derivatives as potential anticancer agents. *European Journal of Medicinal Chemistry*, *108*, 258–273. https://doi.org/10.1016/j.ejmech.2015.11.031

Vega, A. O., Gil, M., & Fernández-Alvarez, E. (1984). Synthesis of 1-hydrazinopyridazino [4, 5-b] quinoxaline and related compounds. *Journal of Heterocyclic Chemistry*, *21*(5), 1271–1276. https://doi.org/10.1002/jhet.5570210505

Vitaku, E., Smith, D. T., & Njardarson, J. T. (2014). Analysis of the structural diversity, substitution patterns, and frequency of nitrogen heterocycles among US FDA approved pharmaceuticals: Miniperspective. *Journal of Medicinal Chemistry*, *57*(24), 10257–10274. https://doi.org/10.1021/jm501100b

Wang, F., Chen, C., Tan, W., Yang, K., & Yang, H. (2016). Structure of main protease from human coronavirus NL63: Insights for wide spectrum anti-coronavirus drug design. *Scientific Reports*, *6*(1), 1–12.

Wu, F., Zhao, S., Yu, B., Chen, Y.-M., Wang, W., Song, Z.-G., Hu, Y., Tao, Z.-W., Tian, J.-H., Pei, Y.-Y., Yuan, M.-L., Zhang, Y.-L., Dai, F.-H., Liu, Y., Wang, Q.-M., Zheng, J.-J., Xu, L., Holmes, E. C., & Zhang, Y.-Z. (2020). A new coronavirus associated with human respiratory disease in China. *Nature*, *579*(7798), 265–269. https://doi.org/10.1038/s41586-020-2008-3

Yoshizawa, S-i., Hattori, Y., Kobayashi, K., & Akaji, K. (2020). Evaluation of an octahydroisochromene scaffold used as a novel SARS 3CL protease inhibitor. *Bioorganic & Medicinal Chemistry*, *28*(4), 115273. https://doi.org/10.1016/j.bmc.2019.115273

Yuan, X.-H., Wang, Y.-C., Jin, W.-J., Zhao, B.-B., Chen, C.-F., Yang, J., Wang, J.-F., Guo, Y.-Y., Liu, J.-J., Zhang, D., Gong, L.-L., & He, Y.-W. (2012). Structure-based high-throughput epitope analysis of hexon proteins in B and C species human adenoviruses (HAdVs). *PLoS One*, *7*(3), e32938. https://doi.org/10.1371/journal.pone.0032938

Yuan, X-h., Wang, Y-c., Qu, Z., Y.; Ren, J-y., Wu, X-m., & Wang, J-f (2013). Phylogenetic and structural analysis of major surface proteins hemagglutinin and neuraminidase of novel avian influenza virus A H7N9 from Chinese patient. *Chemical Research in Chinese Universities*, *29*(5), 934–940. https://doi.org/10.1007/s40242-013-3200-x

Zhang, D., Chen, C.-F., Zhao, B.-B., Gong, L.-L., Jin, W.-J., Liu, J.-J., Wang, J.-F., Wang, T.-T., Yuan, X.-H., & He, Y.-W. (2013). A novel antibody humanization method based on epitopes scanning and molecular dynamics simulation. *PLoS One*, *8*(11), e80636. https://doi.org/10.1371/journal.pone.0080636

Zhang, L., Lin, D., Kusov, Y., Nian, Y., Ma, Q., Wang, J., von Brunn, A., Leyssen, P., Lanko, K., Neyts, J., de Wilde, A., Snijder, E. J., Liu, H., & Hilgenfeld, R. (2020). α-Ketoamides as broad-spectrum inhibitors of coronavirus and enterovirus replication: Structure-based design, synthesis, and activity assessment. *Journal of Medicinal Chemistry*, *63*(9), 4562–4578. https://doi.org/10.1021/acs.jmedchem.9b01828

Zhang, L., Lin, D., Sun, X., Curth, U., Drosten, C., Sauerhering, L., Becker, S., Rox, K., & Hilgenfeld, R. (2020). Crystal structure of SARS-CoV-2 main protease provides a basis for design of improved α-ketoamide inhibitors. *Science (New York, N.Y.)*, *368*(6489), 409–412.